Journal of Materials Chemistry A

PAPER

View Article Online
View Journal | View Issue

Cite this: J. Mater. Chem. A, 2019, 7, 18568

Immobilization of Co, Mn, Ni and Fe oxide co-catalysts on TiO_2 for photocatalytic water splitting reactions†

Jasmin S. Schubert, Janko Popovic, Greta M. Haselmann, Sreejith P. Nandan, Jia Wang, Ariane Giesriegl, Alexey S. Cherevan * and Dominik Eder *

Here we report a systematic study of a series of non-noble-metal co-catalysts based on Co, Mn, Ni and Fe oxides that were prepared by wet impregnation of the corresponding acetylacetonate precursors onto a model TiO_2 substrate, followed by their oxidative decomposition. We analyze thermal evolution of the impregnated $M(acac)_x$–TiO_2 composites with a combination of analytical methods and reveal strong differences in the precursor decomposition onsets and the resulting product composition, compared to the case of pure $M(acac)_x$ precursors. Consequent electron microscopy analyses of the resulting MO_x–TiO_2 composites indicate the presence of small (1–5 nm) amorphous MO_x nanoparticles that are homogeneously distributed on the surface of the substrate TiO_2. Complementing Raman and photoluminescence (PL) spectra confirm pronounced effects of MO_x deposition on the state of TiO_2 substrate and suggest strong electronic communication between the components. The composites obtained at 350 °C were further tested towards sacrificial hydrogen evolution reaction (HER) and oxygen evolution reaction (OER) demonstrating the dynamic nature of the NiO_x–TiO_2 photocatalyst whose Ni^0 active HER sites were generated *in situ* upon light exposure. In contrast, FeO_x–TiO_2, CoO_x–TiO_2, and NiO_x–TiO_2 were all active towards OER, featuring water oxidation ability in descending order, while XPS data of the samples after reaction indicate that partial oxidation of M species takes place during the course of the photocatalytic experiment. This work provides detailed insights on the wet chemistry-based preparation of MO_x co-catalysts decorating oxide nanopowders including optimization of the thermal treatment, potential substrate effects and synergy as well as further prospects in photocatalysis.

Received 27th May 2019
Accepted 18th July 2019

DOI: 10.1039/c9ta05637h

rsc.li/materials-a

Introduction

As of now, renewable energy systems are not mature enough to cover the ever-increasing world energy demands. As a result, the main energy production still comes from non-clean and non-renewable sources, such as fossil fuels, which further contribute to global warming. In addition, the intermittent nature of many renewable energy sources – like in the case of photovoltaics, whose performance depends on the sunlight availability – implies a need for alternative energy storage systems.[1] H_2 has been identified as a promising candidate potentially able to become a base chemical as well as an energy storage system (with its high energy density of 120 MJ kg^{-1} and a non-intermittent supply)[2–4] for our future economy. However, given the fact that the majority of industrial H_2 production is currently still based on natural gas reforming,[5,6] renewable methods of H_2 generation require further development and implementation.

A prodigious approach for clean H_2 production is water splitting, however, in order to induce this reaction using electro- or thermal catalysis, an extensive amount of energy has to be invested.[7] One approach to circumvent this issue relies directly on the renewable energy of sunlight by means of photocatalysis. In this case, the light photons are used to break the water molecules assisted by a photocatalyst, a substance that generates photoexcited charge carriers, delivers them to the solid–liquid interface and catalyzes the redox half-reaction of water oxidation and reduction, the latter yielding the desired H_2 product.[8–10] Although the hydrogen evolution reaction (HER) is given much more attention in the community of heterogeneous photocatalysts,[11] it is the oxygen evolution reaction (OER) that – being kinetically far more complicated (4 electron–4 proton transfer) – often becomes a limiting step for the overall process.

A well-suited model compound for photocatalytic water splitting studies is TiO_2, as it features high chemical stability, shows no toxicity, is cheap, widely available and has a suitable band gap for both half-reactions.[8,9,12–14] However, TiO_2 has several drawbacks that keep it from becoming an efficient water

Institute of Materials Chemistry, Technical University of Vienna, Getreidemarkt 9, Vienna, 1060, Austria. E-mail: alexey.cherevan@tuwien.ac.at; dominik.eder@tuwien.ac.at

† Electronic supplementary information (ESI) available. See DOI: 10.1039/c9ta05637h

splitting photocatalyst.[13,14] These limitations include fast electron–hole recombination rates, poor and unselective catalytic sites on its surface, and a wide band gap that only allows absorption in the UV light range. A number of strategies have been explored to address these issues, such as the use of co-catalysts.[11,13] These surface-attached species (mostly nanoparticles) provide new catalytic sites and simultaneously induce separation of photoexcited electrons and holes.[15] The most widely used co-catalysts are Pt, Pd and IrO_2, RuO_2 for the photocatalytic reduction and oxidation of water, respectively. These are expensive materials based on rare noble metals.[11,16,17] To achieve large scale industrial application of photocatalytic water splitting the development of new co-catalysts based on cheap and widely available elements remains an important issue.

With regard to novel abundant co-catalysts for photocatalytic water splitting, research efforts have focused on d-block transition metals of the fourth period, which are known for their excellent catalytic properties and applications in industry, research and nature.[7,11,14,17] These elements – especially in their oxide form – can undergo quick and reversible redox shuttling, accept, accumulate and release electrons – conditions necessary to generate a self-recovering system. Besides this, their surface structure and chemistry can be varied through synthetic conditions (*e.g.* different oxides can be generated) allowing to further tune adsorption/desorption properties and thus their catalytic function – an aspect rarely investigated so far. For this reason, in this work we explore the nature of Ni, Mn, Co and Fe oxide based co-catalysts and directly compare their potential in both water splitting reactions (OER and HER).

Metal oxide co-catalysts are typically deposited on the photocatalyst surface by sol–gel processes or *via* the use of surfactants.[18–25] These methods allow for a certain degree of control over the size and shape of the co-catalytic species;[19] however, they are often limited when one-pot synthesis is desired. Wet impregnation routes, on the other hand, are simple and cost-effective: for example, by using metal salt impregnation followed by thermal decomposition.[26–29] Although some previous works have reported the synthesis and application of such co-catalyst-loaded TiO_2 powders in photocatalysis,[11,14,17,30–37] many inconsistencies, originating from the wide variety of synthetic and calcination conditions, remain. Furthermore, the lack of comparative activity evaluations leave a gap in the fundamental understanding of their actual active state. Besides these, most of the co-catalysts have been tested solely for HER, and no data on OER performance have been reported.

In order to complement this knowledge gap, in this work, we used a wet impregnation route to prepare Mn, Co, Fe and Ni-based co-catalysts immobilized on TiO_2 nanoparticles (NPs) and systematically investigated their prospects in photocatalytic water splitting reactions. We first analyzed the thermal evolution of pure metal salt precursors and the corresponding composites using thermogravimetric analysis (TGA) and *in situ* X-ray diffraction (XRD) to determine the optimal calcination temperature and product composition. We then elucidated the morphology, crystallinity and oxidation state of the prepared co-catalyst species with a combination of electron microscopy and diffraction as well as XRD, X-ray photoelectron spectroscopy (XPS) and attenuated total reflection Fourier-transform infrared spectroscopy (ATR-FTIR) analyses and correlated these characteristics with their performance towards HER and OER.

Results and discussion

The metal oxide species were synthesized directly on the surface of TiO_2 NPs following the wet impregnation – thermal decomposition method depicted in Fig. 1a. In a typical experiment,

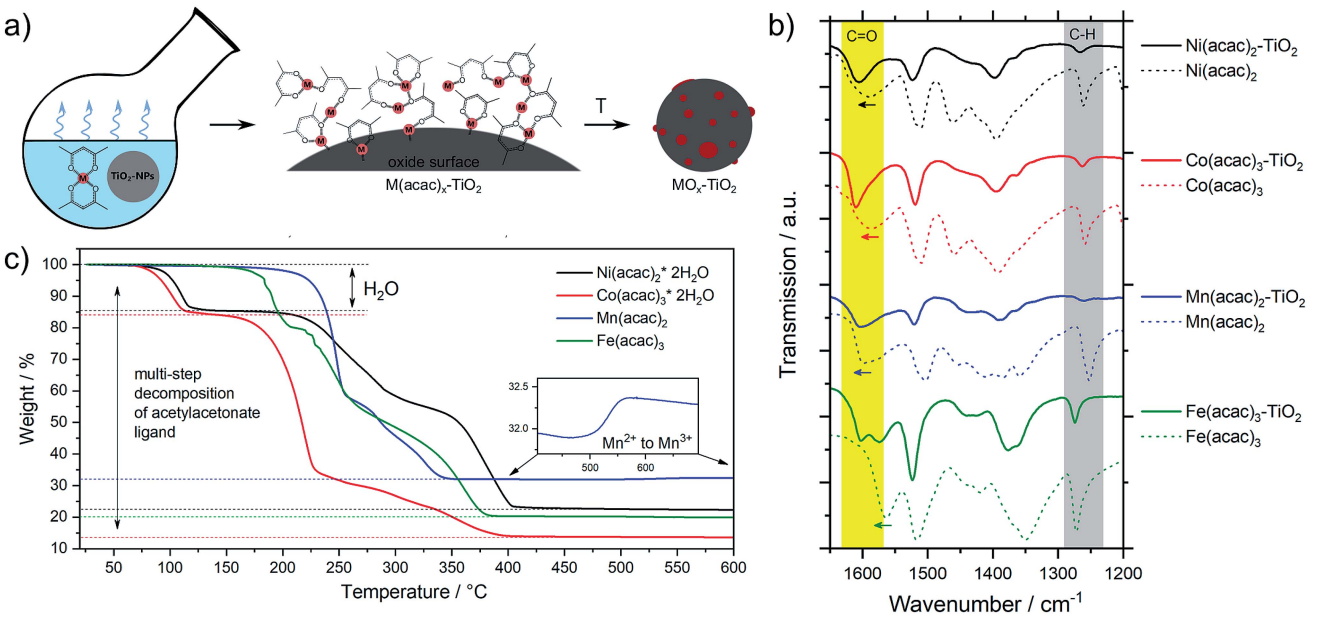

Fig. 1 (a) Schematic description of the synthetic protocol, (b) FTIR spectra of the $M(acac)_x$–TiO_2 composites and the corresponding precursors and (c) TGA data of the pure $M(acac)_x$ precursor salts (heating rate: 5 °C min^{-1} in air; temperature range: 25 °C to 600 °C, M = Fe, Mn, Ni and Co).

a given amount of TiO_2 powder was dispersed in a solvent by ultrasonication, to which a pre-made solution of fully solubilized $M(acac)_x$ species (M = Fe, Mn, Co, Ni; acac = acetylacetonate) was slowly added. The solution was stirred until the solvent was completely evaporated, yielding the corresponding $M(acac)_x$–TiO_2 composites, which were converted into the respective MO_x–TiO_2 composites upon subsequent heat treatment. More details can be found in the Experimental section.

The presence of the $M(acac)_x$ salts in TiO_2 powder after the impregnation can be confirmed by ATR-FTIR spectroscopy (Fig. S1†). The spectra of the composites constitute a superposition of the organic part (most pronounced are ligand-related IR bands) and the TiO_2 substrate (broad absorption below 1000 cm^{-1}), however, a closer look at the 1700–1000 cm^{-1} region (Fig. 1b) indicates that the original peaks of acetylacetonate species are shifted to higher wavenumbers, suggesting a strong binding (chemisorption) of the salt precursors with the substrate material. In addition, the formation of the composites is also apparent from the colour changes – brown, blue, green and red for the Mn, Co, Ni and Fe-based composites, respectively – of the originally white TiO_2 powders observed after impregnation (Fig. S1†).

The composites have been further subjected to thermal treatment in ambient air to oxidatively decompose the metal precursors and yield the corresponding metal oxide co-catalysts on the TiO_2 NPs. However, since there is no consensus in the literature as to which conditions generate which species,[30,31,33,35,36,38–44] we systematically varied the calcination temperature and analysed thermal evolution of both, the pure $M(acac)_x$ precursors and the impregnated $M(acac)_x$–TiO_2 composites.

Thermal analysis

Pure $M(acac)_x$. We first investigated thermal decomposition of pure $M(acac)_x$ precursors. The TGA data in Fig. 1c correspond well to the thermal behaviour observed for similar organic salts reported elsewhere:[45,46] (a) the moderate mass loss at low temperatures (<200 °C) is related to the removal of crystallization water that is present in $Ni(acac)_2$ and $Co(acac)_3$; (b) the large weight loss in the temperature window of 200–400 °C corresponds to the multi-step decomposition of the acetylacetonate species (precursor oxidation).[45] The weight profiles reach a stable plateau after complete salt oxidation, which indicates the formation of stable MO_x species. The only exception is $Mn(acac)_2$, which experiences a small mass gain above 500 °C corresponding well with the partial oxidation of Mn^{2+} to Mn^{3+}.

The TGA data were further complemented by *in situ* XRD using the same heating conditions. Fig. 2 shows that the thermal decompositions of all precursor salts coincide well with the formation of crystalline oxides (full data sets can be found in Fig. S2†).

$Mn(acac)_2$. Fig. 2a shows the characteristic peaks of the original crystal structure of the precursor up to a temperature of about 150 °C, while at 200 °C all diffractions corresponding to the acetylacetonate have vanished, instead showing new diffractions corresponding to Mn_3O_4 (ICDD: 04-007-9641). Both, crystal phase and product composition remain unchanged up to temperatures of around 500 °C, above which the orthorhombic bixbyite Mn_2O_3 appears (ICDD: 04-007-0856), accompanied by corresponding Mn^{2+} oxidation. Both observations are in agreement with TGA (Fig. 1c). Interestingly, no apparent crystal growth is observed for the Mn_3O_4 particles upon calcination at high temperatures, as indicated by the absence of any peak narrowing. Instead, more and more of the Mn^{2+} is oxidized to Mn^{3+} and both oxide phases, Mn_3O_4 and Mn_2O_3, co-exist up to at least 800 °C.

$Co(acac)_3$. The multi-step decomposition of acetylacetonate takes place between 200 and 400 °C according to TGA. The XRD results show that the original crystal structure of the salt

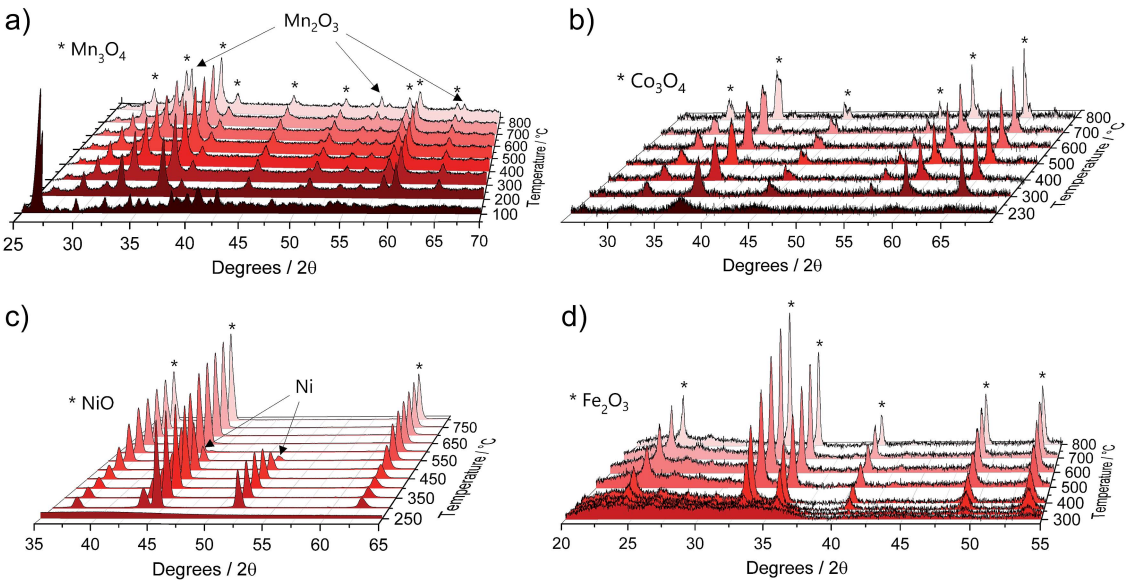

Fig. 2 Selected *in situ* XRD spectra of the pure $M(acac)_x$ (M = Mn, Co, Ni and Fe) precursors acquired in air within a temperature range of 25 °C to 800 °C and heating rate of 5 °C min^{-1} for (a) $Mn(acac)_2$, (b) $Co(acac)_3$, (c) $Ni(acac)_2$ and (d) $Fe(acac)_3$. Full data sets can be found in Fig. S2.†

degrades into an amorphous state already at 100 °C (see Fig. S2†) – temperature at which the removal of crystallization water takes place. At temperatures above 200 °C a broad diffraction at 36.8 degrees – corresponding to crystalline Co_3O_4 (ICDD: 04-014-7747) – appears and gets narrower up to 300 °C indicating gradual growth of the crystallites. The conversion of Co^{3+} species to the mixed-valent oxide is likely induced by the acetylacetonate species through radical formation in a similar way as has been suggested for Cu acetate.[47] No apparent changes in crystal structure take place thereafter up to 800 °C; however, the splitting of the peaks at higher temperatures (>600 °C) may be related to the formation of non-stoichiometric oxides.

Ni(acac)$_2$. The diffractograms in Fig. 2c indicate the formation of a mixed product consisting of metallic Ni (ICDD:04-010-6148) and NiO (ICDD:04-005-4393) in the temperature window of 220–400 °C, which is in agreement with the TGA in Fig. 1c. At temperatures above 250 °C Ni remains the major component up to 500 °C, after which the re-oxidized product starts to dominate the composition. This indicates that the presence of carbonaceous species in metal–organic salt precursors (*e.g.* acetylacetonate) can induce strong Ni^{2+} reduction to purely metallic species during the decomposition phase.[47]

Fe(acac)$_3$. Fig. 2d shows that the decomposition proceeds in a way predicted by TGA. There is no reduction of the metal between 230 and 400 °C, while the single product of rhombohedral hematite Fe_2O_3 (ICDD: 04-002-7501) appears above 300 °C.

These results were further complemented by *quasi in situ* ATR-FTIR performed after subjecting the precursor salts to calcination at different temperatures. The spectra in Fig. S3† confirm that the decomposition of the original acetylacetonates and removal of the intermediate organic species for all composites finish at temperatures above 300 °C.

M(acac)$_x$–TiO$_2$ composites. Next, we investigated the impregnated composites with TGA to see whether the presence of TiO_2 substrate affects the thermal decomposition behavior and the final state of the respective MO_x co-catalyst species.

Interestingly, Fig. 3 not only shows large differences in the decomposition behavior (*e.g.* mechanism of acetylacetonate oxidation), it also indicates strong differences in the decomposition onsets and stability windows (up to 100 °C) for all precursors when impregnated on TiO_2. For example, the $Mn(acac)_2$ species do not undergo a two-step decomposition process within a narrow temperature interval anymore (Fig. 3a compared to Fig. 1c); instead we observe only one strong mass loss in the range between 200 and 250 °C. The final product of decomposition forms already above 250 °C, which is about 100 °C lower than for the pure precursor. In the case of the $Co(acac)_3$–TiO_2, the main weight loss takes place just below 300 °C and likely corresponds to the oxidation of acetylacetonate, which – in the case of the pure precursors – does not finish

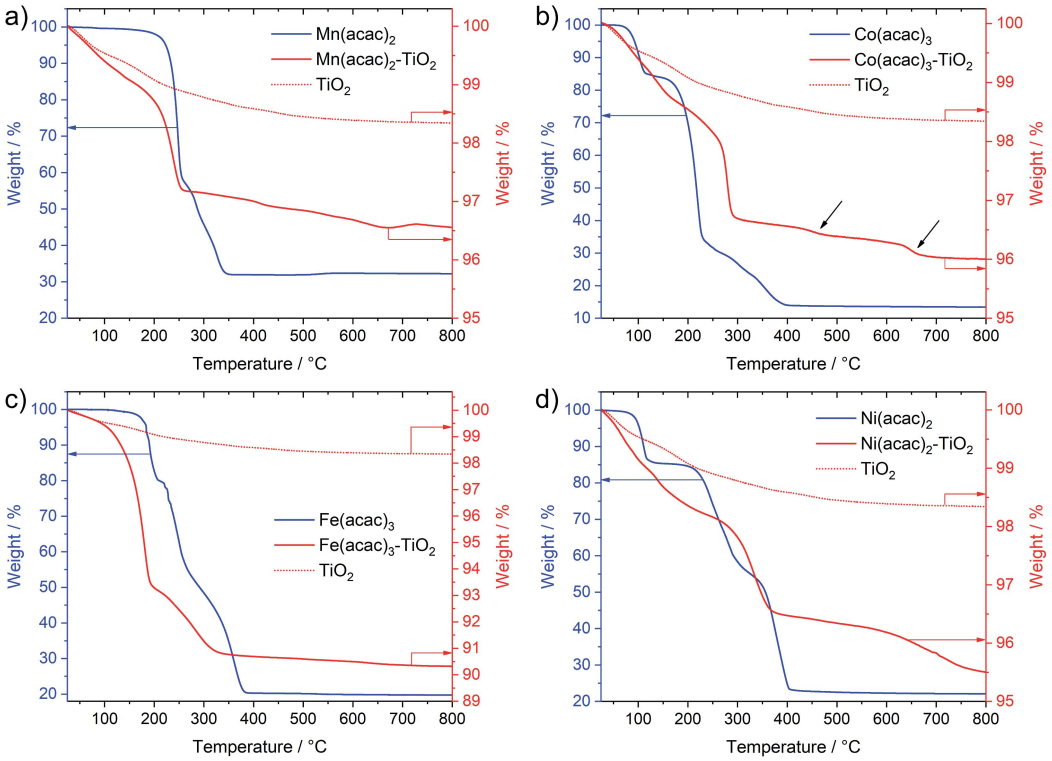

Fig. 3 TGA data of the $Mn(acac)_2$–TiO_2 (a), $Co(acac)_3$–TiO_2 (b), $Fe(acac)_3$–TiO_2 (c) and $Ni(acac)_2$–TiO_2 (d) composites overlapped with that of the pure precursors and the TiO_2 reference. The left *y*-axis corresponds to the weight loss of the pure precursors, the right *y*-axis corresponds to the weight loss of the composite and the reference TiO_2. Data were recorded in air, heating rate 5 °C min^{-1} and in a temperature range from 25 °C to 800 °C. Note the differences in the scale of the *y*-axes. The minor weigh loss observed for the reference TiO_2 in the range from 25 °C to 300 °C is attributed to the presence of physisorbed and chemisorbed species left from the synthesis and processing.

until 400 °C. Besides this, we see at least two additional minor weight losses at roughly 450 °C and 650 °C (see black arrows in Fig. 3b) for the composite with respect to the pure precursor salt.

Similar discrepancies can be observed for the other samples and indeed confirm different kinetics and stages for the decomposition of the immobilized $M(acac)_x$ precursors. More detailed investigations are required to gain full understanding for each individual composite. Our results further suggest that one needs to take care when applying heat treatment protocols, developed for the pure salts, unscrutinized to the corresponding nanocomposites.

After revealing thermal behavior of the impregnated $M(acac)_x$–TiO_2 composites, we have chosen calcination conditions for the thermal treatments aiming to fully decompose the acetylacetonate species, but avoid potential particle growth and possible crystallinity changes of the substrate TiO_2. Considering differences between precursors, an optimum treatment of 350 °C that suited all $M(acac)_x$–TiO_2 samples was applied (see Experimental section) and yielded corresponding NiO_x–TiO_2, MnO_x–TiO_2, CoO_x–TiO_2 and FeO_x–TiO_2 nanocomposites that will be the focus of the following sections.

Morphological investigation

The calcined MO_x–TiO_2 composites were analysed by scanning electron microscopy (SEM) and transmission electron microscopy (TEM). The SEM images in Fig. S4† confirm that the samples are composed of small nanoparticles (NPs) that are similar to the reference TiO_2 (not shown), with no apparent changes in size and shape upon impregnation and calcination. There are also no signs of larger particles, thus we can exclude the formation and growth of unattached MO_x. EDX further indicates a homogeneous distribution of the M elements over the TiO_2 material on the microscale (Fig. S5†). Both observations suggest that no phase segregation upon calcination has occurred and the samples indeed are nanocomposites with M species dispersed across all TiO_2 NPs.

Fig. 4a and b show TEM image of the reference TiO_2 NPs that range between 10 and 50 nm in size and constitute close-to-spherical highly crystalline particles with sharp edges. The electron diffraction (ED) pattern of the reference TiO_2 shows diffuse rings that correspond well to polycrystalline, nanosized anatase and rutile particles (Fig. S6a†). In contrast, TEM images of the composites in Fig. 4 indicate strong changes in surface morphology of the substrate TiO_2 and appearance of surface-attached species.

In the case of MnO_x–TiO_2 (Fig. 4c), the images clearly show the presence of dark spots with sizes between 2 and 5 nm, which likely correspond to the newly formed MnO_x NPs. TEM of the CoO_x–TiO_2 composite in Fig. 4d indicates the presence of smaller 2–3 nm surface-attached CoO_x NPs densely decoration the substrate. A similar morphology is found for NiO_x–TiO_2 (Fig. 4f) where the surface of TiO_2 particles got covered with even smaller (1–2 nm) NiO_x NPs of surprisingly uniform size

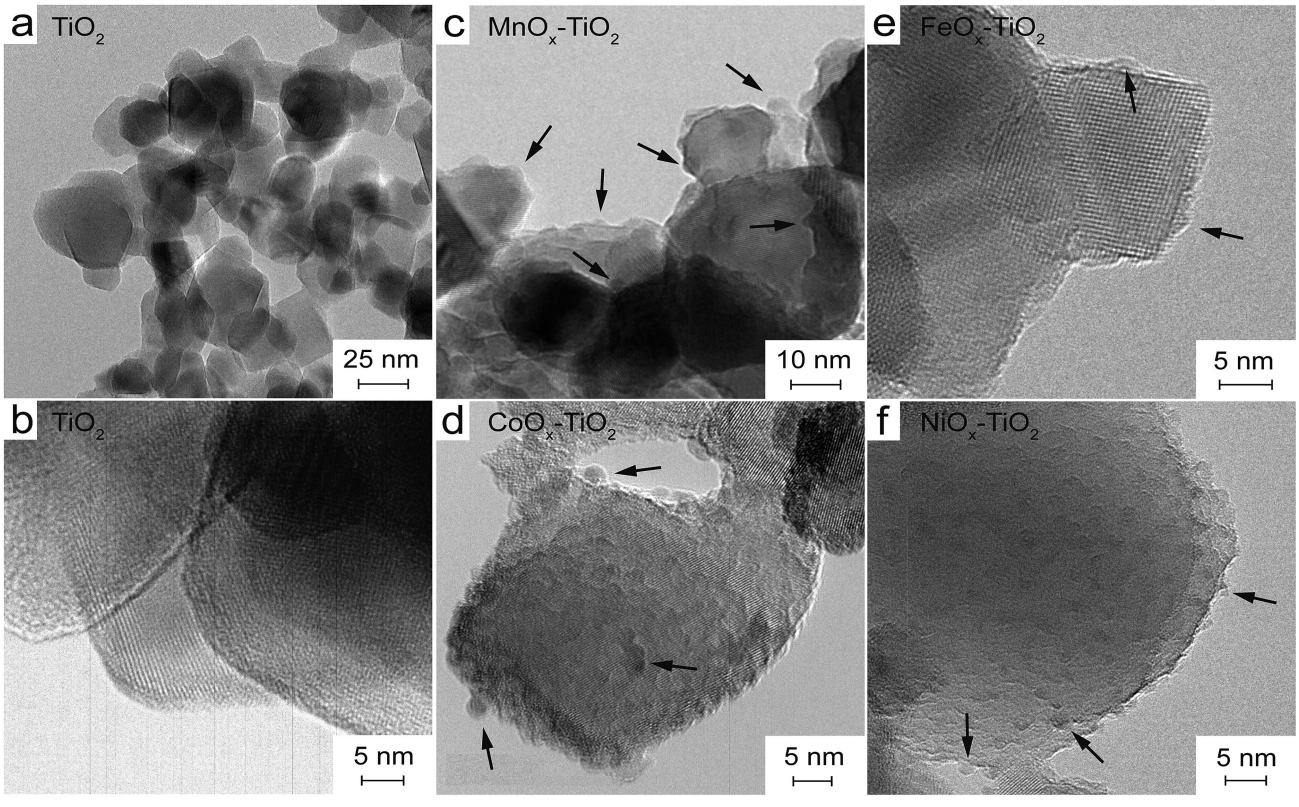

Fig. 4 TEM pictures of the TiO_2 NPs (a and b) as well as MnO_x–TiO_2 (c), CoO_x–TiO_2 (d), FeO_x–TiO_2 (e) and NiO_x–TiO_2 (f) composites prepared at 350 °C. Arrows indicate examples of clearly visible MO_x species.

and shape. For FeO_x–TiO_2 (Fig. 4e), the morphology of the deposits rather resembles a surface shell consisting of small particles sized below 5 nm.

Importantly, we can presently not exclude additional presence of atomic MO_x species on TiO_2 surface, but the majority of the visible MO_x NPs appear to be uniform in size and homogeneously distributed on the surface sharing an intimate interface with the substrate.

Interaction with the matrix

To further elaborate on the state of the MO_x in TiO_2 matrix and on the differences between the composites, we have performed additional Raman and photoluminescence (PL) measurements.

Fig. S7† shows Raman spectra of all as-prepared composites demonstrating that MnO_x–TiO_2, CoO_x–TiO_2 and FeO_x–TiO_2 samples feature strong peak shifts and peak broadening of the anatase-related E_g band with respect to the TiO_2 reference (Table S1†). With regard to our composite systems, these can be assigned to the presence of surface-adsorbed species on TiO_2, creation of O vacancies or even doping with M ions, which cannot be excluded based on ionic radii comparison. In contrast, Raman spectrum of the NiO_x–TiO_2 sample resembles that of the TiO_2 suggesting no strong effect on TiO_2 upon NiO_x immobilization (detailed discussions of Raman data can be found in ESI†).

PL emission spectrum of the substrate TiO_2 powder in Fig. S8† exhibits strong overlapping bands centred at 417, 432 and 461 nm. While the first peak (2.97 eV) can be assigned to band-to-band recombination of rutile component, the latter two (2.87 eV and 2.69 eV) can be attributed to sub-band gap emission characteristic for TiO_2 NPs and related to shallow electronic states associated with *e.g.* oxygen vacancies, structural defects or dopants; in line with Raman results. Spectra of the composites still contain PL peaks of TiO_2, however, they also feature new bands appearing at higher wavelength and characterized by broad emissions centred at 478 nm, 490 nm and 497 nm for the FeO_x–TiO_2, CoO_x–TiO_2 and NiO_x–TiO_2 respectively. The emergence of the additional emission bands at lower energies (2.60 eV, 2.53 eV and 2.49 eV) for all composites can be assigned to the appearance of new relaxation pathways for the carriers originally photoexcited in TiO_2. Judging from TEM and Raman data, one such possibility could be that the electrons or holes are extracted by the surface-attached MO_x species leading to new PL bands related to radiative recombination at MO_x sites or the interface.

This result confirms active electronic communication between the components of the composites and further indicates the ability of the MO_x species to facilitate charge separation in TiO_2.

Crystallinity of the obtained MO_x NPs

Further analysis of the MO_x state and composition with HRTEM has proven to be complicated since the deposited NPs were mostly – with some rare exceptions found in TEM – of amorphous nature. This was further confirmed from the analysis of ED patterns (Fig. S6†) that indicate no additional diffraction spots corresponding to the expected MO_x NPs.

To elucidate more on the amorphous nature of the surface-deposited species in our MO_x–TiO_2 composites, we performed additional XRD measurements (see Fig. S9†). The data in Fig. S9a† shows no diffractions other than that of the TiO_2 substrate for all calcined samples; however, this can also be explained by the low amounts of the MO_x species, thus reaching the detection limit of the XRD technique. To further investigate this, we prepared a set of model samples where the impregnation was done using a much greater amounts of the precursor salts (up to 24.4 wt%) and diffractograms were recorded for the model composites before and after thermal treatment. Still, the XRD did not reveal any peak associated with newly formed oxide species even after calcination (Fig. S9b and c†), thus confirming the TEM and ED data and the conclusion that the MO_x species in the final MO_x–TiO_2 composites are of amorphous nature regardless of the calcination protocol (see ESI for more details†). This amorphous nature of the generated NPs is surprising, because XRD of the pure precursors clearly indicated that the products of the acetylacetonate decomposition, obtained at this calcination temperature, were crystalline (see again Fig. 2). This different behaviour of the composites against the pure precursor is possibly related to surface effects, where TiO_2 restricts the mobility of the surface-bound metallic species and thus prohibits bond rearrangement and formation of a crystalline lattice.

Confirming the oxidation state

Considering the strong differences in the thermal decomposition of the pure precursors and precursors immobilized on the surface of TiO_2, we sought to verify the oxidation state and composition of the surface-deposited species (so far only suggested from *in situ* XRD of pure precursor salts) after thermal treatments using surface-sensitive XPS analyses. Measuring conditions and information about data treatment can be found in the Experimental section.

Survey spectra of all composites are presented in Fig. S10† and reveal the presence of expected elements: Ti and O (mainly from the TiO_2 substrate) as well as Co, Ni, Mn and Fe in the relevant composites. The characteristic C 1s signals correspond very well to adventitious carbon observed in the TiO_2 reference indicating complete decomposition of the acetylacetonate ligand after the applied calcination.[48]

More importantly, Fig. 5 presents the detailed spectra of the Co 2p, Ni 2p, Mn 2p and Fe 2p regions and allows elucidating the oxidation state of the incorporated metals on the surface of TiO_2. XPS analyses of these transition metals is quite complex due to multiplet splitting and different shake-up structures. Thus, the signal of a species can be deconvoluted into various different components that have been analysed in detail previously. This also means that the analysis of the oxidation state of these transition metals is not straight-forward and in some cases can only be seen as indicative. Our analysis is largely based on the work by Biesinger *et al.*[49] Detailed fitting parameters can be found in Table S2.†

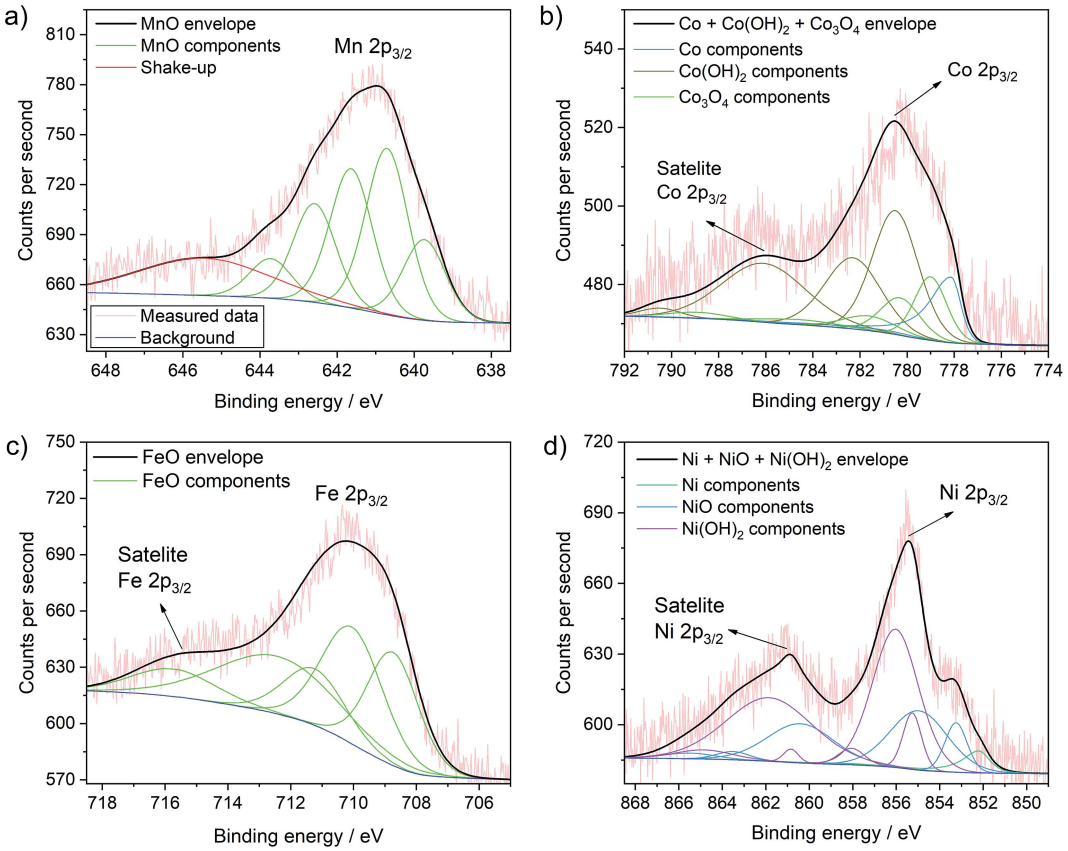

Fig. 5 Detailed XPS spectra of the MnO_x–TiO_2 (a), CoO_x–TiO_2 (b), FeO_x–TiO_2 (c) and NiO_x–TiO_2 (d) samples with the corresponding fits of the different species and mixture of species. Further fits are shown in Fig. S11.†

The Mn 2p spectrum most reliably confirms the presence of Mn^{2+} in the MnO_x–TiO_2 composite (Fig. 5a).[49] We can further clearly exclude the presence of Mn^0 species. Additionally fitting of Mn^{3+} – either from Mn_2O_3 as suggested by XRD, residual precursor salts or due to a partial hydroxylation, *i.e.* MnOOH – result in only a very low percentage (~2%) of the overall signal, which indicates that the concentration of Mn^{3+} – if present at all – is negligible (Fig. S11a and b†). Furthermore, considering multiplet splitting, a Mn^{4+} species is not needed for peak deconvolution.[49] Therefore, we can exclude the presence of Mn^{4+}, in contrast to previous reports on Mn-doped TiO_2.[50,51] In conclusion, Mn^{2+} is the major component in the MnO_x–TiO_2 composite with a negligible contribution of Mn^{3+} due to Mn_2O_3 or MnOOH.

The analysis of the Co 2p signal in Fig. 5b reveals that Co^{2+} and Co^{3+} species coexist in the CoO_x–TiO_2 composite, most likely in the form of oxides, mixed oxide or hydroxides. However, in contradiction to the pure salt XRD and TGA data, we cannot reliably exclude the formation of metallic Co species. The best fit was obtained for a combination of Co metal, $Co(OH)_2$, and Co_3O_4.

In the case of FeO_x–TiO_2 sample, shown in Fig. 5c, the Fe 2p spectrum clearly indicates the presence of Fe^{2+} with a characteristic satellite at 714 eV.[49] From these data, we can suggest that Fe^{3+} is only present as minority species, as we cannot observe pronounced characteristic satellite features at 719 and 735 eV. This supports our previous findings that the thermal evolution of $Fe(acac)_3$ is strongly altered by the TiO_2 substrate resulting in the formation of partially reduced $Fe^{II}O$.

Finally, the XPS data for NiO_x–TiO_2 (Fig. 5d) show mainly Ni^{2+} in the form of NiO or $Ni(OH)_2$. Although not required (Fig. S11c†), the addition of a Ni^0 component improves the fit further and indicates the possible presence of a small fraction of metallic Ni in the final composition, which would also be expected from the data on the pure precursors.[49,52]

In summary, we have produced NiO_x–TiO_2, MnO_x–TiO_2, CoO_x–TiO_2 and FeO_x–TiO_2 composite samples with homogeneously distributed nanoparticles of uniform sizes (2–5 nm) as revealed by electron microscopy and EDX. The results further suggest that the MO_x NPs are of amorphous nature, in contrast to the data on pure precursors, thus indicating substrate effects. XPS analyses shows that Co likely coexists in a mixture of Co^{2+} and Co^{3+}, while major contributors of Mn and Fe species are of +2 oxidation state, again contrary to what has been observed for pure precursors. In the case of NiO_x–TiO_2, XPS additionally indicates a small proportion of metallic species, aside from Ni^{2+}.

Photocatalytic water splitting

We investigated the performance of all samples for photocatalytic water splitting, namely, hydrogen evolution reaction

(HER) and oxygen evolution reaction (OER), by means of sacrificial water splitting. To compare with literature, we used methanol as an electron donor to facilitate HER[53] and $AgNO_3$ as an electron acceptor to support OER.[54,55] Detailed description of the experimental procedure can be found in Experimental section.

Hydrogen evolution reaction

Fig. 6 shows H_2 evolution profiles (on-line H_2 evolution rate *vs.* time) of the as-prepared NiO_x–TiO_2, MnO_x–TiO_2, FeO_x–TiO_2 and CoO_x–TiO_2 composites from water–methanol mixtures under UV light. The results show that only NiO_x–TiO_2 was active towards HER. Hydrogen evolution rates of about 4 μmol h^{-1} were reached after 10 minutes of light exposure in our flow reactor (Fig. S12†). The rest of the composites showed no activity indicating incapability of the generated MnO_x, FeO_x and CoO_x species to act as co-catalysts for H^+ reduction, which is in stark contradiction to some of the literature reports.[34,41]

We have further investigated the active NiO_x–TiO_2 system in long run HER experiments to identify the maximum activity and investigate the performance stability. Fig. 6b shows a HER profile over 60 minutes under illumination: interestingly, no stable evolution rate was reached within this period; instead, the H_2 evolution rate continued to increase, reaching more than 13 μmol h^{-1} at the end of the illumination cycle. We purged the reactor with Ar to remove the reaction products and proceeded with UV illumination for another 14 h. Fig. 6c shows the resulting HER profile revealing two important observations: (a) the activity increased rapidly to a level of 13 μmol h^{-1} within the first hour of illumination, (b) the increase in activity continued in an almost linear fashion to reach rates as high as 27 μmol h^{-1} after 10 h.

This unusual behaviour indicates that either the catalytic sites of the NiO_x–TiO_2 system become more active or their number increases with time. Furthermore, it appears that this behaviour is triggered by light illumination. Although the Ni/NiO system has been investigated as co-catalyst for HER before,[7,11,14,17,56] the question as to which Ni oxidation state is more active remains controversial. Our experimental setup is unique in that it allows for on-line activity detection within the first seconds of light illumination, and our data suggest that the increase in metallic Ni, which can gradually form from Ni^{2+} upon photoreduction, is likely the reason for the observed activity increase.[57] This was confirmed by XPS measurements of the NiO_x–TiO_2 composite recovered immediately after the HER experiment, which revealed a substantial increase in the relative content of Ni^0 compared to Ni^{2+} from 3.4 at% to 16.7 at% at the end of the illumination cycle (Table S3†). To the best of our knowledge, this has not been reported before. The results highlight the dynamics nature of this photocatalyst, and we

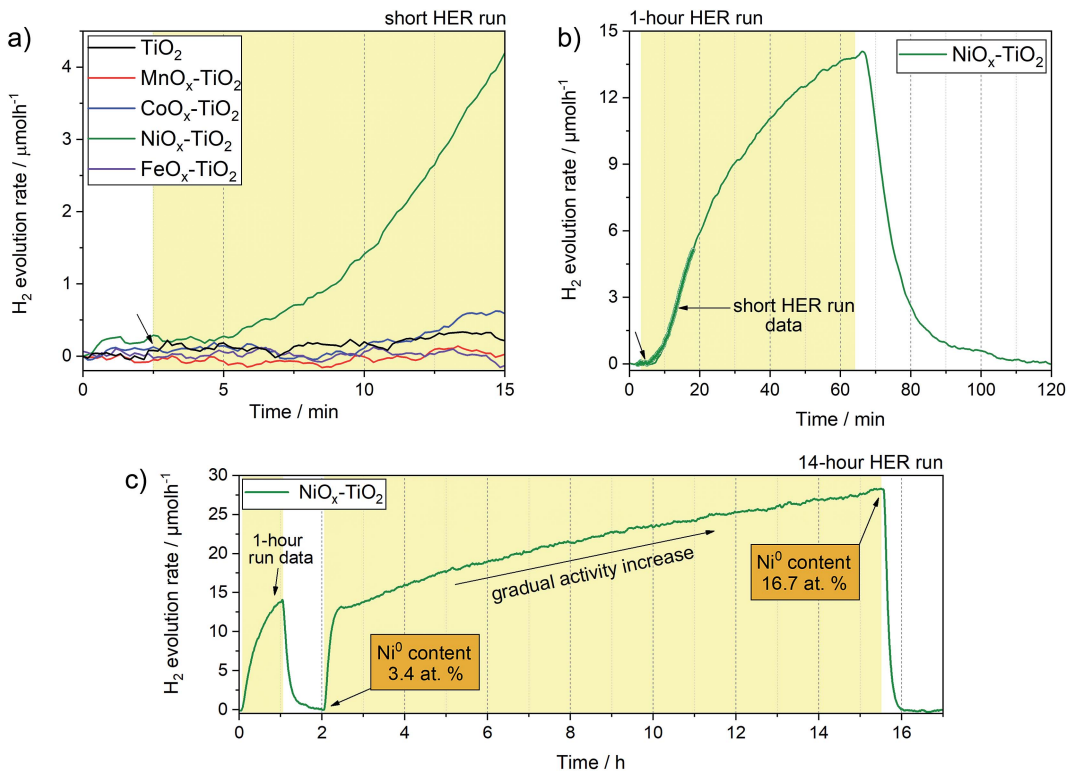

Fig. 6 (a) Short run HER profiles of the NiO_x–TiO_2, MnO_x–TiO_2, FeO_x–TiO_2 and CoO_x–TiO_2 composites along with the reference TiO_2 powder performed using flow-reactor. Arrow indicates the start of illumination, yellow box – illumination period. (b) 1 hour run HER profile of the active NiO_x–TiO_2 photocatalyst along with the corresponding short run data as well as (c) 14 hour run (long run) HER profile showing that the H_2 production rate slowly increases with increasing illumination time. The 1 hour and 14 hour runs have been performed during the same experiment. The reactor was purged with Ar for 1 h in between the runs to remove the reaction products.

emphasize that active species can form upon illumination not only during the first stages of a photocatalytic reaction, but even during extended periods of hours and days.

Based on our TGA, *in situ* XRD and XPS data, we further suggest that NiO_x–TiO_2 composites prepared at lower calcination temperatures (<350 °C) can offer a greater potential for photocatalytic HER as they preserve a higher fraction of metallic Ni species.

Oxygen evolution reaction

We have further tested the composites towards OER previously rarely reported for these series of co-catalysts. Again, we followed the typical conditions for sacrificial OER and used $AgNO_3$ as an electron acceptor as well as a closed reactor system (see Experimental section and Fig. S12†). Fig. 7a reveals that three of the composite photocatalysts were active towards water oxidation, namely, FeO_x–TiO_2, CoO_x–TiO_2 and NiO_x–TiO_2, with the corresponding O_2 evolution rates reaching 34.3, 31.4 and 19.9 μmol h^{-1} after 20 min of illumination, respectively (see Fig. 7b). Noteworthy, pure TiO_2 powder without being loaded with any co-catalyst also exhibited respectable OER performance with the rate of 20.8 μmol h^{-1}, suggesting that surface of bare TiO_2 – with Ti^{4+} in d^0 type configuration – also provides suitable sites for water oxidation.[58] In contrast to other samples, the OER on TiO_2 was completely suppressed in the case of the MnO_x–TiO_2 composite.

Enhanced OER rates recorded in the presence of surface-attached CoO_x and FeO_x species can be ascribed to their active role in facilitating the charge separation and/or acting as water oxidation sites; in line with other literature reports where Co- and Fe-oxide-based co-catalysts have been shown to possess some photo- or electrocatalytic activity towards water oxidation.[11,59–63] To further elaborate on the active state and stability of these OER-active co-catalysts, we performed XPS measurements after the OER experiments (see ESI†). Fig. S13a† clearly suggests that some of the initial Fe^{2+} species of the FeO_x–TiO_2 composite oxidized during the photocatalytic process resulting in a higher proportion of Fe^{3+}, as can be seen from the appearance of the characteristic satellites at 719 and 737 eV. Nevertheless, judging from the stable rate of O_2 evolution in Fig. 7a, we can suggest that no severe activation/deactivation process has taken place during the reaction and Fe^{2+} can still be considered as one of the OER-active components of the composite. With regard to CoO_x–TiO_2, XPS data of the sample after OER (Fig. S13b†) show that oxidation of the initially present Co species takes place during the photocatalytic reaction without any apparent activity loss. This suggests that high-oxidation state Co species are likely to be responsible for the OER performance. Elucidation of this question will require further dedicated investigations.

In the case of the NiO_x–TiO_2 composite, we observed no apparent increase in OER rate compared to bare TiO_2, despite the fact that NiO – that is present in our composite – and various Ni oxyhydroxides are known for their excellent water oxidation performance.[64,65] However, it has also been reported, that performance of Ni-based co-catalysts is strongly dependent on the calcination conditions and may need to be optimized to obtain desired OER rates. Nevertheless, the as-prepared NiO_x–TiO_2 composite containing both metallic Ni and NiO can be considered as a promising candidate for overall water splitting as it contains both HER and OER sites whose initial ratio can be controlled during the synthesis.

The rather negative result obtained for the MnO_x–TiO_2 case (Fig. 7b) can be related to well-known sensitivity of Mn-based oxides OER performance to their structure and Mn oxidation state.[66] Our XPS data suggest that the MnO_x co-catalyst NPs are mainly composed of Mn^{2+}, while a number of literature reports suggest that the presence of Mn^{3+} and Mn^{4+} is required for the accumulation of the required oxidizing equivalents necessary to drive water oxidation.[67,68] Judging from our TGA and *in situ* XRD data, we could suggest that much higher calcination temperatures (>600 °C) will be required to produce MnO_x species with higher content of Mn in higher oxidation states, that could be of interest for photocatalytic OER.

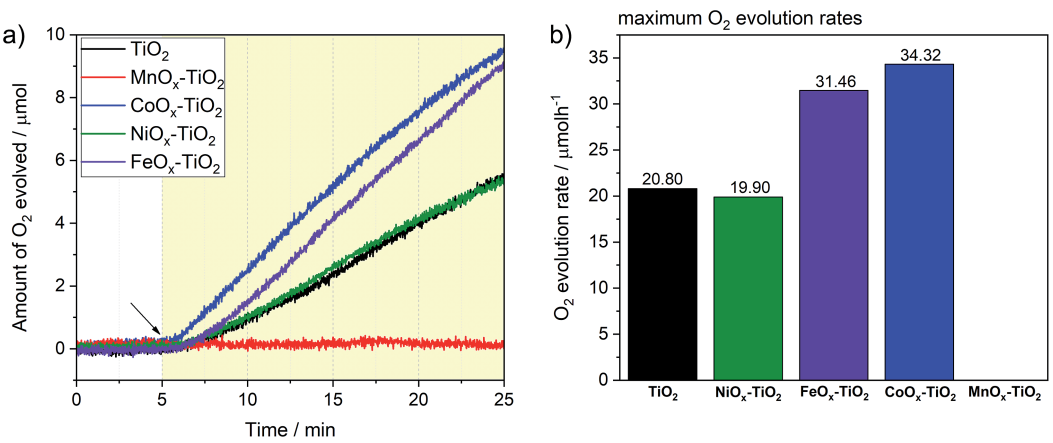

Fig. 7 (a) OER evolution profiles for the NiO_x–TiO_2, MnO_x–TiO_2, FeO_x–TiO_2 and CoO_x–TiO_2 composites along with the reference TiO_2 powder performed using a closed reactor. The arrow indicates start of illumination. The coloured area corresponds to the illumination period. (b) Bar chart presenting maxima of O_2 evolution rates extracted from derivative analysis.

Conclusions

In this contribution, we systematically studied a series of NiO_x–TiO_2, MnO_x–TiO_2, CoO_x–TiO_2 and FeO_x–TiO_2 photocatalysts prepared by wet impregnation of $M(acac)_x$ salts (M = Ni, Fe, Mn and Co) onto high surface area TiO_2 NP substrate, followed by their oxidative decomposition. A combination of TGA, *in situ* XRD, ATR-FTIR as well as XPS revealed strong differences in thermal decomposition of the $M(acac)_x$–TiO_2 in comparison to pure $M(acac)_x$ salts. When loaded on TiO_2, the M precursors undergo decomposition at substantially lower temperatures, *via* different mechanism and often result in the formation of otherwise unstable M species, such as Fe^{2+} in the case of FeO_x–TiO_2. Consequent SEM and TEM analyses along with EDX mappings showed that the morphology of the created MO_x–TiO_2 composites feature small (1–5 nm) MO_x NPs homogeneously decorating the TiO_2 NPs. In addition, XRD and ED suggested that the MO_x co-catalysts prepared at 350 °C are of amorphous nature, while combined Raman and PL spectra indicate the possibility of M doping and strong electronic communication between the components of the composites.

We further evaluated the potential of the composites towards photocatalytic water splitting reactions. We show that among all samples, NiO_x–TiO_2 was active towards hydrogen evolution reaction (HER) with metallic Ni species – gradually generated *in situ* upon light illumination – being the active site. In contrast, FeO_x–TiO_2, CoO_x–TiO_2, and NiO_x–TiO_2 were all active towards oxygen evolution reaction (OER), featuring water oxidation ability in descending order. XPS data of the OER-active samples after reaction indicated that mild oxidation of M species takes place during the course of the photocatalytic experiment. However, Fe^{2+} species could still be considered as one of the OER-active components of the FeO_x–TiO_2 composite.

This contribution provides a systematic study on the specifics of the wet chemistry-based synthesis of small MO_x NPs directly onto the surface of TiO_2, which can be expanded to other inorganic substrates. Besides, we show that some of the prepared catalysts are of interest for photocatalytic water splitting reactions and that their activity could be further controlled by modifying synthetic conditions.

Experimental section

Chemicals

All materials used for the syntheses were obtained from commercial suppliers. As such, P25 TiO_2 from Degussa, $Mn(acac)_2$ from Sigma-Aldrich (99.8% pure), $Co(acac)_3 \cdot 3H_2O$ from Fluka (99.9% pure), $Ni(acac)_2 \cdot 2H_2O$ from Sigma-Aldrich (99.8% pure) and $Fe(acac)_3$ from Sigma-Aldrich (97% pure). The used solvent for the syntheses were deionized water and absolute ethanol (from Chem-Lab NV) and for photocatalytic experiments deionized water and HPLC-gradient grade methanol (from VWR).

Synthesis of the composites

The metal oxide species were synthesized directly on the surface of TiO_2 NPs following the wet impregnation – thermal decomposition method depicted in Fig. 1a. The general synthesis procedure used for all samples included (a) suspending the TiO_2 powder (400 mg, 5 mmol) in 20 mL of ethanol; (b) stirring the suspension for 10 minutes; (c) adding the corresponding precursor salt: $Mn(acac)_2$ (0.248 mmol, 62.7 mg), $Co(acac)_3$ (0.297 mmol, 75.6 mg), $Ni(acac)_2$ (0.113 mmol, 29.1 mg), or $Fe(acac)_3$ (0.26 mmol, 92.0 mg); and (d) subjecting the resulting suspension to sonication to assist salt dissolution and homogenisation of the suspension components. The resulting mixture was left stirring at 60 °C until complete evaporation of the solvent. The remaining powder was then dried at 80 °C for 5 h and grinded. Afterwards, the samples were heat-treated at 350 °C for 10 h in ambient air to generate the corresponding oxides resulting in MO_x–TiO_2 composites.

Characterisation methods

Scanning electron microscopy (SEM) images were acquired using FEI Quanta 250 FEG at 200 keV scanning electron microscope to obtain visual information on the morphology of the samples. Typically acceleration voltage of 2 kV and secondary electron detection mode were used. Energy dispersive X-ray spectroscopy (EDX) was performed using the SEM to obtain elemental maps.

Transmission electron microscopy (TEM) images were obtained using FEI TECNAI F20 transmission electron microscope equipped with a field emission gun in bright field mode using 200 kV acceleration voltage. The sample was prepared from a suspension in ethanol without ultrasonication, using a copper holey carbon coated grids (Plano, 200 mesh).

X-ray diffraction (XRD) was performed using an XPERT III: PANalytical XPert Pro MPD (Θ–Θ Diffractometer) for the *in situ* experiments and an XPERT II: PANalytical XPert Pro MPD (Θ–Θ Diffractometer) for the *ex situ* experiments. The sample was placed on a sample holder and irradiated with a Cu X-ray source (8.04 keV, 1.5406 Å). The signal was acquired with Bragg–Brentano Θ/Θ-diffractometer geometry ranging from 5° to 80° degrees. The detector system was a semiconductor X'Celerator (2.1°) detector. The *in situ* experiment was performed under air flow and temperatures ranging from 25 °C to 800 °C.

The thermogravimetric (TGA) measurements were carried out on a PerkinElmer Thermogravimetric Analyser TGA 8000. The samples were placed into an Al_2O_3 crucible and heated with a dynamic method at a heating rate of 5 °C min^{-1} under air from 25 °C to 800 °C.

The chemical composition of the samples was obtained with X-ray photoelectron spectroscopy (XPS) using a custom-built SPECS XPS-spectrometer equipped with a monochromatised Al-K_α X-ray source (μ 350) and a hemispherical WAL-150 analyser (acceptance angle: 60°). All samples were mounted onto the sample holder using double-sided carbon tape. Pass energies of 100 eV and 30 eV and energy resolutions of 1 eV and 100 meV were used for survey and detail spectra, respectively (excitation energy: 1486.6 eV, beam energy and spot size: 70 W onto 400 μm, angle: 51° to sample surface normal, base pressure: 5×10^{-10} mbar, pressure during measurements: 2×10^{-9} mbar). To reduce charging effects, a broad-spot low energy

electron source (SPECS FG 22 flood gun, 8–12 eV/15–30 μA) was used for charge compensation in some samples (containing Mn and Fe). Data analysis was performed using CASA XPS software, employing transmission corrections (as per the instrument vendor's specifications), Shirley backgrounds and Scofield sensitivity factors. Charge correction was applied so the adventitious carbon peak (C–C peak) was shifted to 284.8 eV binding energy (BE). All content values shown are in units of relative atomic percent (at%), where the detection limit in survey measurements usually lies around 0.1–1 at%, depending on the element. For the attenuated total reflection Fourier-transform infrared spectroscopy (ATR-FTIR) measurements a PerkinElmer FTIR Spectral UATR-TWO with a spectrum two Universal ATR (Single Reflection Diamond) accessory was used.

Fluorescence steady state measurements of the TiO_2 and MO_x–TiO_2 NPs were carried out using PicoQuant FluoTime 300 spectrophotometer. For PL spectra, the excitation source was Coaxial UV-Xe arc lamp (ozone free – with 300 W power) coupled with a computer-controlled double-grating monochromator and the detection system comprised of PMA Hybrid 07 detector and a high resolution emission double monochromator. For all the measurements, the excitation wavelength was kept to be the 377 nm (corresponding to 3.29 eV photon energy), and the PL data was collected using the EasyTau2 software.

Raman measurements were conducted with LabRAM HR800 from Horiba. Ne:YAG diode was used as the 532 nm laser source and the characteristic Raman peak of Si at 520.8 cm^{-1} was used as the calibration peak. The laser intensity was keep at 5 mW.

Photocatalytic experiments

Hydrogen evolution experiments were performed using a top irradiation gas-flow slurry type home-made reactor equipped with a LED lamp light source centred at 365 nm (Thorlabs). In a single experiment, 10 mg of a powdered photocatalyst was dispersed in 50 mL 50 vol% MeOH–water solution by stirring. During the experiment, the reactor was continuously purged with argon (flow rate of 30 mL min^{-1}, controlled with a mass flow controller from MCC-Instruments) to deliver the gaseous products to the online gas analyzer (X-Stream, Emerson Process Management) equipped with a thermal conductivity detector (TCD) for H_2 quantification. The temperature of the reactor was kept constant through a water cooling system (Lauda). In a single experiment, the suspension was first stirred for 30 min in the dark, then illuminated for 15 min. A typical H_2 evolution profile (*e.g.* in Fig. 6) obtained with our flow reactor includes an "induction" period (increasing H_2 evolution rate during the first 5–10 min) that is due to the fact the H_2 gas first needs to fill the dead volume (*e.g.* reactor volume, tubing volume) to reach the detector. When the illumination is stopped, the signal returns to its baseline. The H_2 evolution rates were normalized by subtracting the H_2 evolution rate measured in the blank experiment (no catalyst present in the MeOH–H_2O mixture) as a result of UV-assisted MeOH oxidation (photo-reforming).

Oxygen evolution experiments were performed in a home-made top illumination closed reactor using the same light source and water cooling system. The experiments were carried out using a 2 mL water solution containing 1 mg of a photocatalyst (dispersed *via* stirring) and $AgNO_3$ (0.1 M) as electron scavenger. The reactor was first purged with Ar to remove the air and the O_2 detection was started using a fibre-optic oxygen sensor (PyroScience) inserted in the reaction volume. The suspension was stirred for 30 min in the dark to allow for O_2 signal stabilization followed by 20 minutes of UV illumination.

Conflicts of interest

There are no conflicts to declare.

Acknowledgements

The authors would like to acknowledge facilities of the Vienna University of Technology for technical support and fruitful discussions: X-Ray Center (XRC) and especially Werner Artner and Klaudia Hradil; Analytical Instrumentation Center (AIC) and especially Markus Sauer and Annette Foelske-Schmitz; Electron Microscopy Center (USTEM) and especially Karin Whitmore and Johannes Bernardi.

Notes and references

1 H. Ibrahim, A. Ilinca and J. Perron, *Renewable Sustainable Energy Rev.*, 2008, **12**, 1221–1250.
2 K. T. Møller, T. R. Jensen, E. Akiba and H. Li, *Prog. Nat. Sci.: Mater. Int.*, 2017, **27**, 34–40.
3 S. E. Hosseini and M. A. Wahid, *Renewable Sustainable Energy Rev.*, 2016, **57**, 850–866.
4 P. Millet, in *Hydrogen Production*, John Wiley & Sons, Ltd, 2015, pp. 63–116.
5 M. Serban, M. A. Lewis, C. L. Marshall and R. D. Doctor, *Energy Fuels*, 2003, **17**, 705–713.
6 B. E. Logan, *Environ. Sci. Technol.*, 2004, **38**, 160A–167A.
7 I. Roger, M. A. Shipman and M. D. Symes, *Nat. Rev. Chem.*, 2017, **1**, 0003.
8 *Nanocomposites for Visible Light-induced Photocatalysis*, ed. M. M. Khan, D. Pradhan and Y. Sohn, Springer International Publishing, 2017.
9 Photocatalysis,https://www.crcpress.com/Photocatalysis-Principles-and-Applications/Ameta-Ameta/p/book/9781482254938, accessed January 22, 2019.
10 J. Schneider, D. Bahnemann, J. Ye, G. L. Puma and D. D. Dionysiou, *Photocatalysis: Fundamentals and Perspectives*, Royal Society of Chemistry, 2016.
11 X. Li, J. Yu, J. Low, Y. Fang, J. Xiao and X. Chen, *J. Mater. Chem. A*, 2015, **3**, 2485–2534.
12 A. O. Ibhadon and P. Fitzpatrick, *Catalysts*, 2013, **3**, 189–218.
13 M. Ni, M. K. H. Leung, D. Y. C. Leung and K. Sumathy, *Renewable Sustainable Energy Rev.*, 2007, **11**, 401–425.
14 T. Jafari, E. Moharreri, A. S. Amin, R. Miao, W. Song and S. L. Suib, *Molecules*, 2016, **21**, 900.
15 Z. Zhang and J. T. Yates, *Chem. Rev.*, 2012, **112**, 5520–5551.
16 T. Kawai and T. Sakata, *J. Chem. Soc., Chem. Commun.*, 1980, 694–695.

17 B. M. Hunter, H. B. Gray and A. M. Müller, Earth-Abundant Heterogeneous Water Oxidation Catalysts, *Chem. Rev.*, 2016, **116**(22), 14120–14136.
18 Sol-Gel Derived Nanomaterials and It's Applications, https://www.researchgate.net/publication/288630167_Sol-Gel_Derived_Nanomaterials_and_It's_Applications_A_Review, accessed January 22, 2019.
19 R. Nagarajan and T. Alan Hatton, *Nanoparticles: Synthesis, Stabilization, Passivation, and Functionalization*, American Chemical Society, 2008, vol. 996, pp. i–v.
20 H. Chen, X. Y. Liu, X. D. Hao and Y. X. Zhang, *Ceram. Int.*, 2016, **42**, 19425–19428.
21 P. Praveen, G. Viruthagiri, S. Mugundan and N. Shanmugam, *Spectrochim. Acta, Part A*, 2014, **120**, 548–557.
22 W. Xin, D. Zhu, G. Liu, Y. Hua and W. Zhou, *Synthesis and Characterization of Mn–C–Co-doped Nanoparticles and Photocatalytic Degradation of Methyl Orange Dye under Sunlight Irradiation*, https://www.hindawi.com/journals/ijp/2012/767905/, accessed January 22, 2019.
23 C. Karunakaran, P. Vinayagamoorthy and J. Jayabharathi, *Superlattices Microstruct.*, 2013, **64**, 569–580.
24 Y. Wan, Z. Xu, W. Chao and J. Zhang, *J. Exp. Nanosci.*, 2013, **8**, 782–787.
25 W. Liu, Z. Liu, G. Wang, X. Sun, Y. Li and J. Liu, *Sci. China Mater.*, 2017, **60**, 438–448.
26 S. G. Babu, P. Karthik, M. C. John, S. K. Lakhera, M. Ashokkumar, J. Khim and B. Neppolian, *Ultrason. Sonochem.*, 2019, **50**, 218–223.
27 A. M. Antolín, S. Contreras, F. Medina and D. Tichit, *Top. Catal.*, 2017, **60**, 1156–1170.
28 T. Harifi and M. Montazer, *Appl. Catal., A*, 2014, **473**, 104–115.
29 J. Lasek, Y.-H. Yu and J. C. S. Wu, *Environ. Technol.*, 2012, **33**, 2133–2141.
30 J.-D. Lin, S. Yan, Q.-D. Huang, M.-T. Fan, Y.-Z. Yuan, T. T.-Y. Tan and D.-W. Liao, *Appl. Surf. Sci.*, 2014, **309**, 188–193.
31 J. Yu, Y. Hai and B. Cheng, *J. Phys. Chem. C*, 2011, **115**, 4953–4958.
32 A. T. Montoya and E. G. Gillan, *ACS Omega*, 2018, **3**, 2947–2955.
33 P. D. Tran, L. Xi, S. K. Batabyal, L. H. Wong, J. Barber and J. S. C. Loo, *Phys. Chem. Chem. Phys.*, 2012, **14**, 11596–11599.
34 J. Si, S. Xiao, Y. Wang, L. Zhu, X. Xia, Z. Huang and Y. Gao, *Nanoscale*, 2018, **10**, 2596–2602.
35 H. Tada, Q. Jin, H. Nishijima, H. Yamamoto, M. Fujishima, S. Okuoka, T. Hattori, Y. Sumida and H. Kobayashi, *Angew. Chem., Int. Ed.*, 2011, **50**, 3501–3505.
36 H. Yu, H. Irie, Y. Shimodaira, Y. Hosogi, Y. Kuroda, M. Miyauchi and K. Hashimoto, *J. Phys. Chem. C*, 2010, **114**, 16481–16487.
37 A. Li, T. Wang, X. Chang, W. Cai, P. Zhang, J. Zhang and J. Gong, *Chem. Sci.*, 2016, **7**, 890–895.
38 M. Higashi, K. Domen and R. Abe, *J. Am. Chem. Soc.*, 2012, **134**, 6968–6971.
39 A. Singh, S. L. Y. Chang, R. K. Hocking, U. Bach and L. Spiccia, *Energy Environ. Sci.*, 2013, **6**, 579–586.
40 W.-T. Chen, A. Chan, D. Sun-Waterhouse, T. Moriga, H. Idriss and G. I. N. Waterhouse, *J. Catal.*, 2015, **326**, 43–53.
41 W. Wang, S. Liu, L. Nie, B. Cheng and J. Yu, *Phys. Chem. Chem. Phys.*, 2013, **15**, 12033–12039.
42 H. Yu, J. Tian, F. Chen, P. Wang and X. Wang, *Sci. Rep.*, 2015, **5**, 13083.
43 Z. Yan, X. Yu, Y. Zhang, H. Jia, Z. Sun and P. Du, *Appl. Catal., B*, 2014, **160–161**, 173–178.
44 M. Nolan, A. Iwaszuk and H. Tada, *Aust. J. Chem.*, 2012, **65**, 624–632.
45 B. Pal and M. Sharon, *Thin Solid Films*, 2000, **379**, 83–88.
46 S. A. Sadeek, *An. Asoc. Quim. Argent.*, 2005, **93**, 165–176.
47 Z. Lin, D. Han and S. Li, *J. Therm. Anal. Calorim.*, 2012, **107**, 471–475.
48 T. L. Barr and S. Seal, *J. Vac. Sci. Technol., A*, 1995, **13**, 1239–1246.
49 M. C. Biesinger, B. P. Payne, A. P. Grosvenor, L. W. M. Lau, A. R. Gerson, R. St and C. Smart, *Appl. Surf. Sci.*, 2011, **257**, 2717–2730.
50 M. Chandra Sekhar, B. Purusottam Reddy, S. V. Prabhakar Vattikuti, G. Shanmugam, C.-H. Ahn and S.-H. Park, *J. Cluster Sci.*, 2018, **29**, 1255–1267.
51 Q. R. Deng, X. H. Xia, M. L. Guo, Y. Gao and G. Shao, *Mater. Lett.*, 2011, **65**, 2051–2054.
52 M. C. Biesinger, B. P. Payne, L. W. M. Lau, A. Gerson and R. S. C. Smart, *Surf. Interface Anal.*, 2009, **41**, 324–332.
53 J. K. Stolarczyk, S. Bhattacharyya, L. Polavarapu and J. Feldmann, *ACS Catal.*, 2018, **8**, 3602–3635.
54 R. Niishiro, R. Konta, H. Kato, W.-J. Chun, K. Asakura and A. Kudo, *J. Phys. Chem. C*, 2007, **111**, 17420–17426.
55 G. Hitoki, T. Takata, J. N. Kondo, M. Hara, H. Kobayashi and K. Domen, *Chem. Commun.*, 2002, 1698–1699.
56 W. Zhang, Y. Li, X. Zeng and S. Peng, *Sci. Rep.*, 2015, **5**, 10589.
57 I. Majeed, M. A. Nadeem, E. Hussain, G. I. N. Waterhouse, A. Badshah, A. Iqbal, M. A. Nadeem and H. Idriss, *ChemCatChem*, 2016, **8**, 3146–3155.
58 J. Sato, N. Saito, H. Nishiyama and Y. Inoue, *J. Phys. Chem. B*, 2001, **105**, 6061–6063.
59 F. Meng, J. Li, S. K. Cushing, J. Bright, M. Zhi, J. D. Rowley, Z. Hong, A. Manivannan, A. D. Bristow and N. Wu, *ACS Catal.*, 2013, **3**, 746–751.
60 N. Zhang, J. Shi, S. S. Mao and L. Guo, *Chem. Commun.*, 2014, **50**, 2002–2004.
61 D. M. Jang, I. H. Kwak, E. L. Kwon, C. S. Jung, H. S. Im, K. Park and J. Park, *J. Phys. Chem. C*, 2015, **119**, 1921–1927.
62 M. Okazaki, Y. Wang, T. Yokoi and K. Maeda, *J. Phys. Chem. C*, 2019, **123**, 10429–10434.
63 M. S. Burke, S. Zou, L. J. Enman, J. E. Kellon, C. A. Gabor, E. Pledger and S. W. Boettcher, *J. Phys. Chem. Lett.*, 2015, **6**, 3737–3742.
64 H. Kato and A. Kudo, *J. Phys. Chem. B*, 2001, **105**, 4285–4292.
65 C. K. Mavrokefalos and G. R. Patzke, *Inorganics*, 2019, **7**, 29.
66 R. Pokhrel, M. K. Goetz, S. E. Shaner, X. Wu and S. S. Stahl, *J. Am. Chem. Soc.*, 2015, **137**, 8384–8387.
67 M. Wiechen, M. M. Najafpour, S. I. Allakhverdiev and L. Spiccia, *Energy Environ. Sci.*, 2014, **7**, 2203–2212.
68 P. Kurz, *Top. Curr. Chem.*, 2016, **371**, 49–72.